

Hot Electrons and Bound State Potential at Plasmon Boundaries

M. Akbari-Moghanjoughi¹

¹*Faculty of Sciences, Department of Physics,
Azarbaijan Shahid Madani University, 51745-406 Tabriz, Iran**

(Dated: October 23, 2020)

Abstract

Current research presents a model of half-space plasmon excitations for electron gas of arbitrary degeneracy in a homogenous ambient neutralizing positive background. The half-space plasmon excitations in current linearized Schrödinger-Poisson model reveals some interesting features. This is due to the fact that it benefits an effective dual length-scale character of quantum plasmon excitations, simultaneously, taking into account the high phase-speed collective excitations due to electrostatic interactions in the electron fluid and low phase-speed phenomenon caused by single electron excitations. The mutual coupling between these length scales is remarked to lead to the formation of well defined miniature periodic density fringes in the excited electron fluid which are modulated over the envelop density and potential patterns. The later interaction leads to formation of a hot electron packet outside the physical jellium boundary of the system. The potential energy exterior to surface gives rise to a bound state potential valley in parametric density-temperature region relevant to the metallic surfaces, which resembles those of the surface binding potentials. This effect may be appropriate to explain the Casimir-Polder-like forces between parallel metallic plates in vacuum and metallic nanoparticle interactions. We also use the model to describe the hot electron generation in plasmonic band structure. Current model can be further extended to explore characteristic features of plasmon excitations in other geometries like spherical for investigation of short range interactions among nanoparticles and to better understand the photocatalytic properties of nanometals.

PACS numbers: 52.30.-q, 71.10.Ca, 05.30.-d

*Corresponding author: massoud2002@yahoo.com

I. INTRODUCTION

Plasmonics [1, 2] is a new interdisciplinary field with important applications in nano-electronics [3, 4], optoelectronics [5], and semiconductor integrated circuit industry [6–11]. Plasmons are elementary collective excitation of quantum plasmas which play an inevitable role in nature [12–18]. These entities provide ideal platform for fast THz device communications [19] and beyond where the conventional wired communications fail to operate. Plasmonic energy conversion is an alternative way of solar power extraction in future photovoltaic and catalytic designs due to their much higher efficiency compared to semiconductor technologies [20–27]. The state of the art nanocatalytic engineering for energy extraction is based on conversion of energy of collective surface electron plasma oscillations caused by localized electromagnetic radiation into hot electron generation in plasmonic devices which operates in ultraviolet-visible (UV-VIS) frequency range. However, the conventional solar cell devices are based on low energy interband electron-hole transitions in semiconductors which operate at visible-near infrared (VIS-NIR) low frequency range. However, plasmonic devices operating in ultraviolet spectrum in the wavelength range (10 – 380)nm requires special technological considerations and nanofabrication costs [28] due to low contribution of plasmonic device operation range to the solar radiation spectrum. Recent studies have revealed that nanostructured materials can be used to directly convert collected electromagnetic energy into electricity by local surface plasmon resonance (LSPR) in the hot electron generation mechanism [29]. The generated hot electrons are then collected by putting the metallic nanoparticles in contact with a good electron acceptor like TiO_2 in Schottky configuration [30]. Studies also reveal that hot electron extraction efficiency is strongly dependent on the size and geometry of nanoparticles as well as their composition [31].

Quantum plasma regime ranges from doped semiconductors [32, 33] with moderately high electron number density at low temperature and high density metallic compounds up to high-temperature and density called warm dense matter (WDM) [34, 35]. Quantum effect arise naturally when the interspecies distances exceeds the thermal de Broglie wavelength [36]. In inertial confinement fusion experiment quantum effects vary in strength due to change in equation of state (EoS) of matter during shock compression causing increase in temperature and number density [37]. The change of EoS has one fundamental quantum effect on the faith of compact stellar object setting distinct limit on the mass of such entities [38]. Another

quantum feature of charged particle ensemble is their complex collective electromagnetic interactions even with their average interparticle distances below the quantum limit. The later is because of nonlocal nature of interactions acting via the Bohm's quantum diffraction potential. This is why a dilute electron gas interaction with crystal lattice can lead to distinct quantum effects in Bragg diffraction phenomenon [39, 40]. The development of quantum plasmas had a long history with many pioneering contributions over the past century [41–50]. Because of the dominant quantum effects caused by the EoS of a Fermi gas, semiclassical plasma theories which incorporate the quantum statistical pressure effects but ignore the electron nonlocality still lead to many interesting features [51–56]. However, many old quantum plasma theories based on the standard Thomas-Fermi assumptions which ignore the von Weizsacker gradient corrections to kinetic energy [57] as the main root to collective nonlocal behavior of an electron gas, fail to capture the full essence of quantum many-body effects.

There has been an increasing interest in the quantum plasma theories over the recent decade due to their effective description of collective quantum features [58–69]. Quantum kinetic [70], quantum (magneto)hydrodynamic [71] and gradient corrected density functional theory (DFT) has been used to investigate different aspects of many particle interactions in plasmas. Application of the simplest one, i.e. quantum hydrodynamic approach, has led to discovery of many fascinating collective properties of plasmas which has not been discovered in old theories due to ignorance of quantum electron diffraction phenomenon. The quantum hydrodynamic theory may also be cast into the form of well-known single particle Madelung fluid theory using the appropriate transformations on statistical quantities. The use of such framework, so-called Schrödinger-Poisson model [72], has the power to study variety of interesting linear and nonlinear features of plasmonic environments [73–75] with the least complexity and computational cost. Recently, the pseudoforce system derived from linearized Schrödinger-Poisson model has been used to study some novel features of plasmon excitations [76]. This new model has a fundamental property of taking into account the dual lengthscale nature of single-particle as well as collective interactions in a single frame. The use of linearized quantum hydrodynamic model has recently led to some controversies on the novel attractive potential between quantum screened ions due to the wavenumber scale mismatch in conventional model [77–86]. It has been shown that energy dispersion of plasmon excitations consists of two main branches each representing different high and low

phase-speed phenomena in plasmonics [87–93]. The attractive quantum screening potential obtained in linearized quantum hydrodynamic framework has also been shown to be the ground state plasmonic effect in Schrödinger-Poisson model.

II. THE MATHEMATICAL MODEL

In order to study the plasmon excitations in an arbitrary degenerate electrostatically interacting electron gas we assume an ambient jellium-like neutralizing background of positive ions and use the following one-dimensional Schrödinger-Poisson model [76]

$$i\hbar \frac{\partial \mathcal{N}}{\partial t} = -\frac{\hbar^2}{2m} \frac{\partial^2 \mathcal{N}}{\partial x^2} - e\phi \mathcal{N} + \mu(n, T) \mathcal{N}, \quad (1a)$$

$$\frac{\partial^2 \phi}{\partial x^2} = 4\pi e(|\mathcal{N}|^2 - n_0), \quad (1b)$$

in which $\mathcal{N} = \sqrt{n(x, t)} \exp[iS(x, t)/\hbar]$ is the state function of the electron gas in the jellium model with $\mathcal{N}\mathcal{N}^* = n(x, t)$ characterizing the number density and $v(x, t) = (1/m)\partial S(x, t)/\partial x$ the speed of fluid. Also, ϕ is the collective electrostatic field due to all charges in the system and n_0 is the background charge density. Moreover, $\mu(n, T)$ is the chemical potential of the gas defined through the generalized equation of state (EoS) for isothermal electron gas with arbitrary degree of degeneracy.

For our case the electron EoS relates the fundamental thermodynamic quantities such as the statistical pressure and the number density to the chemical potential μ and the electron temperature T as

$$n = -\mathcal{D} \text{Li}_{3/2}[-\exp(\beta\mu)], \quad P = -\frac{\mathcal{D}}{\beta} \text{Li}_{5/2}[-\exp(\beta\mu)], \quad (2)$$

in which $\beta = 1/k_B T$ and \mathcal{D} is so-called the effective electron density of states [32]

$$\mathcal{D} = \frac{2}{\Lambda^3} = 2 \left(\frac{m}{2\pi\beta\hbar^2} \right)^{3/2}, \quad (3)$$

with the parameter Λ being the electron thermal de Broglie wavelength. The EoS (2) is also conveniently written in a more compact structure

$$P = \frac{n \text{Li}_{5/2}[-\exp(\beta\mu)]}{\beta \text{Li}_{3/2}[-\exp(\beta\mu)]}, \quad (4)$$

where the polylogarithm function is defined in terms of the Fermi functions

$$\text{Li}_\nu(-e^z) = -\frac{1}{\Gamma(\nu)} \int_0^\infty \frac{x^{\nu-1}}{\exp(x-z)+1} dx, \quad \nu > 0, \quad (5)$$

and Γ being the ordinary gamma function.

Note that the EoS can be expanded in terms of the limiting cases of non-degenerate (classical) and fully degenerate limits. For the fully degenerate isothermal electron gas, $z \gg 1$, one obtains the form $\lim_{z \rightarrow \infty} \text{Li}_\nu(-e^z) = -z^\nu/\Gamma(\nu + 1)$ while in the extreme opposite non-degenerate limit, $z \ll -1$, one gets $\text{Li}_\nu(-e^z) \approx -e^z$. It is evident that in the complete degeneracy limit (such as in metals) the equation of state becomes $P = (2/5)nk_B T_F$ in which $T_F = E_F/k_B$ is the electron Fermi temperature with $E_F = \hbar^2(3\pi^2 n)^{2/3}/(2m)$ being the Fermi energy of the completely degenerate (zero temperature) electron gas where \hbar denotes the scaled Planck constant, whereas, in the non-degenerate limit we retain $P = nk_B T$ for a classical dilute electron gas.

Here we intend to use the model for metallic compounds with highly degenerate electrons and strongly coupled ions (jellium model). The defining parameter for degeneracy is $\eta = T/T_F$ in which T and T_F are respectively the electron fluid and Fermi temperatures. Therefore, the parametric regime $\eta < 1$ ($\eta > 1$) denotes the degenerate (nondegenerate) electron fluid. For fully degenerate metals and metallic nanoparticles we have the extreme case of $\eta \ll 1$ or $T_F \gg T$. In elemental metals at room temperature the Fermi temperature amounts to about 10^4K or higher depending on their electron concentrations. In this limit the chemical potential equals the Fermi energy and all electrons reside below the well defined Fermi level. On the other hand, ion dynamic properties are characterized via the ion coupling parameter, $\Gamma = Ze^2/dk_B T_i$, in which d is the average inter-ion distance and T_i is the ion temperature being much lower compared to that of electron fluid $T_i \ll T_e$ due to the large fractional mass ratio. A good criteria for the weak and strong coupling cases are $\Gamma \ll 1$ and $\Gamma \gg 1$, respectively [94]. Therefore, metallic compounds with $r_s = 2 - 6$, where $r_s = d/r_B$ is the Bruckener parameter and r_B is the Bohr radius, are categorized as strongly coupled material possessing ionic crystal lattice. However, in current jellium ion model we ignore the effect of lattice vibrations (phonons) on electronic properties of the electron gas. Moreover, the electron fluid with $r_s \ll 10^{-2}$ is regarded as nonrelativistic electron gas while semiconductors have the parameter value of $r_s > 25$. Because for semiconductors the Fermi temperature is close to that of the electron fluid, they are regarded as partially degenerate electron fluid. The electron degeneracy starts approximately at number density of $n \simeq 10^{18}\text{cm}^{-3}$. However, in doped semiconductors the electron density can be much lower than this critical value. In fully degenerate elemental metals the electron concentration is

typically in the range $(10^{21} - 10^{23})\text{cm}^{-3}$.

We intend to study the system (1) in the linear limit for simplicity in current analysis. Such a simplified model ignoring other minor interaction effects such as the electron exchange and correlations still provides many interesting collective features of the electron system. Appropriately normalized closed model constitute of a coupled time-independent system of coupled differential equation

$$\frac{d^2\Psi(x)}{dx^2} + \Phi(x) + 2E\Psi(x) = 0, \quad (6a)$$

$$\frac{d^2\Phi(x)}{dx^2} - \Psi(x) = 0, \quad (6b)$$

where it has been assumed that $\mathcal{N}(x, t) = \psi(x)\psi(t)$ for the purpose of variables separation and $\Psi(x) = \psi(x)/\sqrt{n_0}$ and $\Phi(x) = e\phi(x)/2E_p$ with $E_p = \hbar\sqrt{4\pi e^2 n_0/m}$ being the plasmon energy of the system. Also, $E = (\epsilon - \mu_0)/2E_p$ with ϵ being the eigenenergy of the system is defined through $\epsilon\psi(t) = \hbar\omega\psi(t) = i\hbar d\psi(t)/dt$ with ω being the eigenfrequency of plasmon oscillations. Note that the space and time variables are also normalized, respectively, to the plasmon length $1/k_p$ with $k_p = \sqrt{2mE_p}/\hbar$ being the plasmon wavenumber and \hbar/E_p . Note also that we have used the Thomas-Fermi assumption for the chemical potential in fully degenerate limit where this potential is supposed to be constant throughout the system in the linear approximation. However, for the Bose-Einstein condensate or in a nonlinear charged system this quantity may vary considerably, so that the local electrostatic potential may not cancel the variations in the chemical potential. The dual-tone solution to (6) is

$$\begin{bmatrix} \Phi_g(x) \\ \Psi_g(x) \end{bmatrix} = \frac{1}{2\alpha} \begin{bmatrix} \Psi_0 + k_2^2\Phi_0 & -(\Psi_0 + k_1^2\Phi_0) \\ -(\Phi_0 + k_1^2\Psi_0) & \Phi_0 + k_2^2\Psi_0 \end{bmatrix} \begin{bmatrix} \cos(k_1x) \\ \cos(k_2x) \end{bmatrix}, \quad (7)$$

where Φ_0 and Ψ_0 denote the wave functional values at the origin and the characteristic wavenumbers k_1 and k_2 are given as

$$k_1 = \sqrt{E - \alpha}, \quad k_2 = \sqrt{E + \alpha}, \quad \alpha = \sqrt{E^2 - 1}. \quad (8)$$

The interesting complementarity-like relation $k_1k_2 = 1$ characterizes the connection between the wave and particle aspects of plasmon excitations. The solution (8) leads to the generalized energy dispersion $E = (1 + k^4)/2k^2$ in which E and k are normalized to $2E_p$ and plasmon wavenumber k_p , respectively. The solution (7) reminds the de Broglie's double solution proposed of the pilot-wave theory [95] in which a single electron may be assumed

to be guided by the collective electrostatic interactions in the electron gas. The pilot wave theory has gained a renewed interest with many experimental support [96] over the past few years.

The one-dimensional model of plasmon excitations in electron gas (6) has been generalized to the damped pseudoforce system in order to include the charge screening effect or other similar many-body effects [89].

$$\frac{d^2\Psi(x)}{dx^2} + 2\xi\frac{d\Psi(x)}{dx} + \Phi(x) + 2E\Psi(x) = 0, \quad (9a)$$

$$\frac{d^2\Phi(x)}{dx^2} + 2\xi\frac{d\Phi(x)}{dx} - \Psi(x) = 0, \quad (9b)$$

where $\xi = k_{sc}/k_p$ with the normalized screening parameter $\xi^2 = (E_p/2n_0)\partial n/\partial\mu = (1/2\theta)\text{Li}_{1/2}[-\exp(2\mu/\theta)]/\text{Li}_{3/2}[-\exp(2\mu/\theta)]$ being the one-dimensional screening wavenumber in the finite temperature Thomas-Fermi model [89] with $\theta = T/T_p$ being the normalized temperature of the electron gas and $T_p = E_p/k_B$ being the characteristic plasmon temperature. The solution to damped pseudoforce system (9) is

$$\Phi_d(x) = \frac{e^{-\xi x}}{2\alpha} \left\{ \begin{array}{l} (k_2^2\Phi_0 + \Psi_0) \left[\cos(\beta_1 x) + \frac{\xi}{\beta_1} \sin(\beta_1 x) \right] - \\ (k_1^2\Phi_0 + \Psi_0) \left[\cos(\beta_2 x) + \frac{\xi}{\beta_2} \sin(\beta_2 x) \right] \end{array} \right\}, \quad (10a)$$

$$\Psi_d(x) = \frac{e^{-\xi x}}{2\alpha} \left\{ \begin{array}{l} (\Phi_0 + k_2^2\Psi_0) \left[\cos(\beta_2 x) + \frac{\xi}{\beta_2} \sin(\beta_2 x) \right] - \\ (\Phi_0 + k_1^2\Psi_0) \left[\cos(\beta_1 x) + \frac{\xi}{\beta_1} \sin(\beta_1 x) \right] \end{array} \right\}, \quad (10b)$$

where $\beta_1 = \sqrt{k_1^2 - \xi^2}$ and $\beta_2 = \sqrt{k_2^2 - \xi^2}$. The initial values $\Psi_0(x)$ and $\Phi_0(x)$ are related through a universal relation $\Phi_0 = \gamma\Psi_0$ with $\gamma = 2\hbar\sqrt{\pi/m}$ at plasmon boundaries between two environments [92].

Figure 1 shows variations of the characteristic plasmon parameters for the electron gas of arbitrary degeneracy. Figure 1(a) depicts the variations of normalized one-dimensional damping parameter $\xi(\mu, \theta)$ in terms of the normalized chemical potential μ for various values of the normalized plasmon temperature, θ . It is remarked that with increase in the chemical potential of the gas the damping parameter decreases substantially. In the model of one-dimensional screened surface it might be interpreted that with increase in the degeneracy degree at given electron temperature the screening length increases, while it seems contradictory, since when plasma density increases the Debye length always decreases. However, for the normalized screening parameter, ξ , with the scaling parameter as k_p which is directly

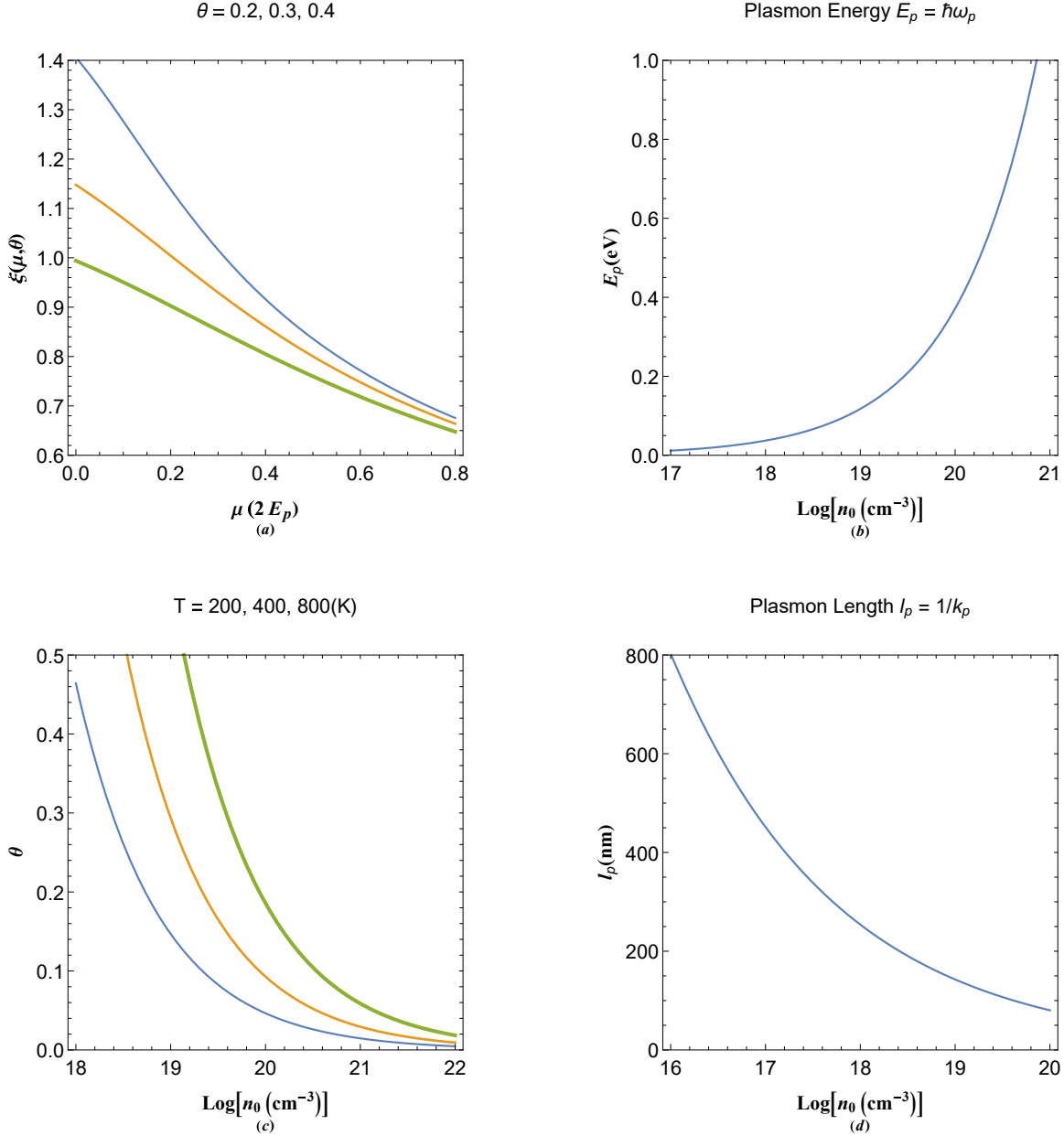


FIG. 1: 1(a) The variation of normalized screening (damping) parameter as a function of normalized chemical potential for different values of normalized electron temperature, θ . 1(b) Variation in the plasmon energy in terms of electron number density in logarithmic scale. 1(c) Variations of normalized electron temperature in terms of electron number density for different values of the normalized electron temperature. 1(d) The plasmon length variation in terms of the electron number density. The increase in the thickness of curves in each plot is meant to represent an increase in the varied parameters above each panel.

related to the electron number density, the decrease in this parameter is convincing. It is also seen that as the normalized temperature increases, variations in ξ over the chemical potential range decreases. The figure also shows that for the case of complete degeneracy the dependence of the normalized damping parameter to θ becomes insignificant. Moreover, Fig. 1(b) shows the variation in plasmon energy in terms of electron number density in a logarithmic scale. It is remarked that the increase in plasmon energy becomes sharp as the degeneracy limit, ($n_0 \simeq 10^{18}\text{cm}^{-3}$), sets in. For typical metals the plasmon energy amounts a few electron Volts. For instance, for cesium with the plasmon energy as low as $E_p \simeq 2.9\text{eV}$ it can reach much higher value for aluminium with $E_p \simeq 15\text{eV}$. However, in order to compare the screening effect in these the difference in their chemical potential which is their Fermi energy at zero-temperature limit ($E_F^{Cs} = 1.59\text{eV}$, $E_F^{Al} = 11.7\text{eV}$) must be taken into account. Figure 1(c) depicts the variations in the fractional temperature θ as a function of the electron number density for various electron fluid temperatures. It is seen that for a given electron temperature value the normalized electron temperature decreases significantly with increase in the electron number-density. The variation in this parameter gets even more significant when the electron temperature increases. It is remarked that in the complete degeneracy limit dependence of this parameter to electron temperature becomes insignificant. Figure 1(d) shows the variation in the plasmon length in terms of the electron number density in nanometer scale. It is remarked that this characteristic length decreases sharply with increase in the electron number density with values as high as few tenth of micrometers for semiconductors to values as low as few nanometers in metallic densities.

III. MODEL OF HALF-SPACE PLASMON EXCITATIONS

To this end, let us consider the case in which the electron gas bounded in a half-space ($x < 0$). For simplicity, we ignore the dynamics of ions of the jellium and their screening effect. Therefore, there is a sharp discontinuity at $x = 0$. For the half-space $x > 0$ there exists a small fraction of electron spill-out due to damped plasmon excitations in vacuum as continuation of the electron gas in $x < 0$ region. Therefore, the complete solution of the system consists of $\Psi(x) = \Psi_{<}(x) + \Psi_{>}(x)$ and $\Phi(x) = \Phi_{<}(x) + \Phi_{>}(x)$ where $\Psi_{>}(x) = \Psi_d$ ($\Phi_{>}(x) = \Phi_d$) and $\Psi_{<}(x) = \Psi_g$ ($\Phi_{<}(x) = \Phi_g$).

Figure 2 shows the variations in normalized perturbed electron number-density, $n(x) =$

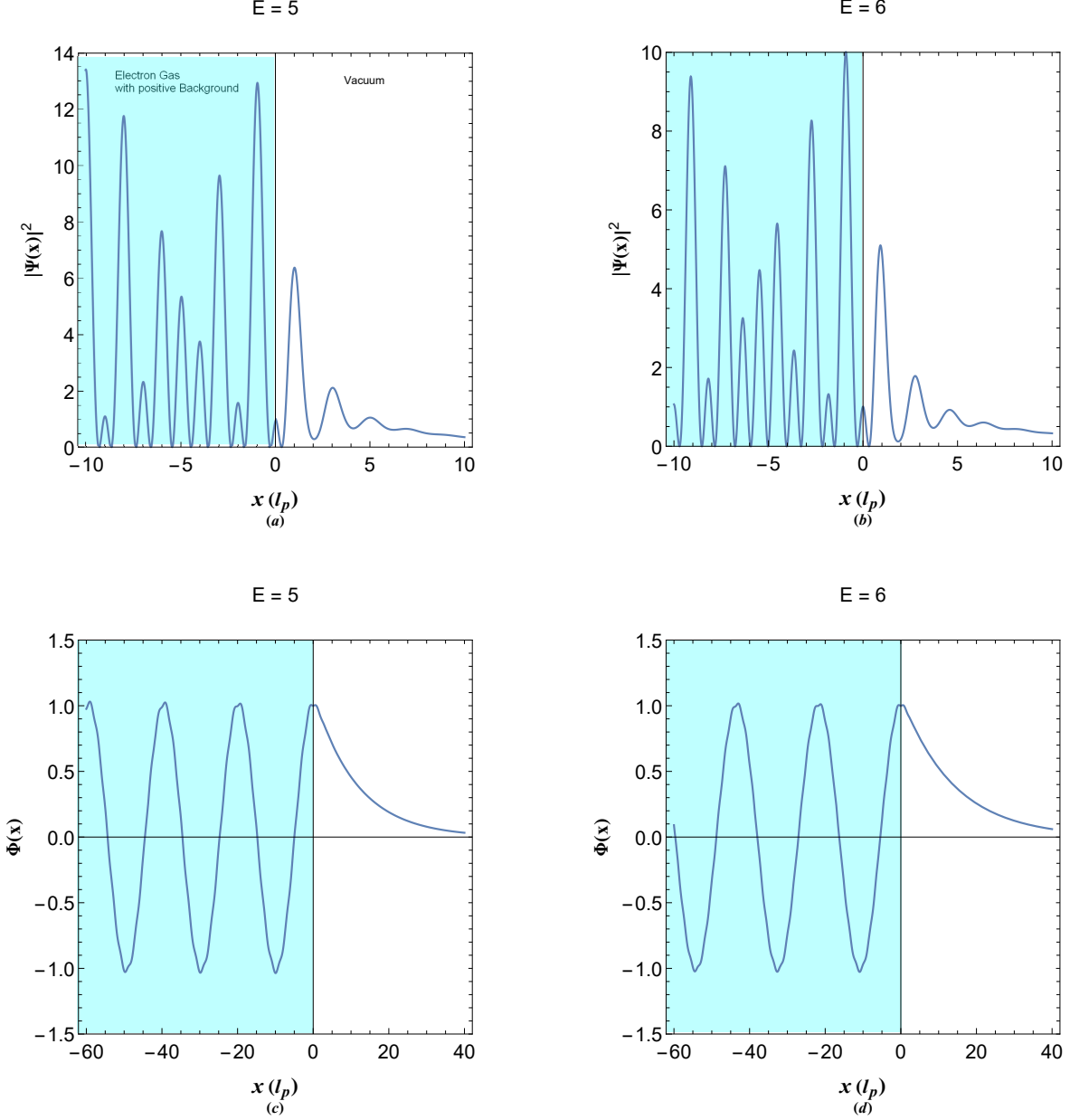


FIG. 2: Profiles of normalized perturbed electron number-density and electrostatic potential energy for electron gas-vacuum half-space plasmon excitations at given energy eigenvalue shown above each panel. The boundary at $x = 0$ separates the electron gas (shaded area) from the vacuum (unshaded region).

$\Psi(x)\Psi^*(x)$, and electrostatic potential energy, $\Phi(x)$, for the electron gas region for different values of the energy eigenvalues. It is clearly evident that the values and derivatives of state functions must match at the half-space boundary. As remarked in Figs. 2(a) and 2(b), for $x < 0$ there are double-tone oscillations in electron probability density, $\Psi(x)$,

and consequently in electron number density. Meanwhile, in the region $x > 0$ there is an exponential decrease in amplitude of density variations accompanied with rapid oscillations in the structure. In Fig. 2(b) the increase in energy eigenvalue leads to relative decrease in the density profile. Variations in the electrostatic energy of the system is shown in Figs. 2(c) and 2(d). It seems that the variations in the region $x < 0$ for $\Phi(x)$ is regular as compared to that of $\Psi(x)$. The plasmonic oscillations are of double-wavenumber character with the smaller wavelength scale corresponding to the single particle behavior and the larger one to collective behavior in the electron gas. It is therefore seen that modulated oscillation amplitude in electrostatic energy of the electron gas caused by single particle effects is comparably lower and is shown as small variations modulated over a larger oscillatory pattern cause by the collective behavior of the gas. However this is not the case for the probability density $\Psi(x)$ in which the modulated oscillations are profound as compared to those of the electrostatic energy profile. On the other hand, for $x > 0$ the electrostatic energy decay has approximately pure exponential form without oscillations. In fact such oscillations exist have insignificant effect on amplitudes not detected over a large scale. Figure 2(d) reveals that unlike for the case of number density, increase of energy eigenvalue does not significantly alter the amplitude of electrostatic energy profile. However in the region $x > 0$ the decay rate for lower energy eigenvalue of Fig. 2(c) is slightly higher compared to that of the high energy eigenvalue shown in Fig. 2(d).

The state functionals, $\Psi(x)$ and $\Phi(x)$ provide sufficient information in order to calculate thermodynamic quantities at an equilibrium state. We need however to know the statistical plasmon energy distribution and plasmon density of states (DoS) in order to obtain the statistically averaged quantities

$$\langle \Phi(\mu, \theta, x) \rangle = \frac{\int_1^{\infty} \Phi(E, \mu, \theta, x) f(E, \mu, \theta) D(E) dE}{\int_1^{\infty} f(E, \mu, \theta) D(E) dE}, \quad (11a)$$

$$\langle \Psi(\mu, \theta, x) \rangle = \frac{\int_1^{\infty} \Psi(E, \mu, \theta, x) f(E, \mu, \theta) D(E) dE}{\int_1^{\infty} f(E, \mu, \theta) D(E) dE}, \quad (11b)$$

$$\langle n(\mu, \theta, x) \rangle = |\langle \Psi(\mu, \theta, x) \rangle|^2, \quad (11c)$$

where $f(E) = [\exp(2E/\theta) - 1]^{-1}$ is the Bose-Einstein occupation number and $D(E)$ is the

plasmon energy DoS given as [87]

$$D(E) = \frac{\sqrt{E(4E^2 - 3) + (4E^2 - 1)\sqrt{E^2 - 1}}}{2\pi^2\sqrt{E^2 - 1}}. \quad (12)$$

Note that the DoS used here is different from that in Refs. [87, 89]. This is because in current calculations we use the modified plasmon dispersion, $E = (1 + k^4)/2k^2$ in which E is normalized to $2E_p$, whereas, in Refs. [87, 89] the dispersion $E = (1 + k^4)/k^2$ has been used in which the energy is normalized to E_p . Consequently, the lower integration limits differ in later cases.

Figure 3 depicts the spatial distribution of normalized perturbed electron number-density and electrostatic energy for given normalized chemical potential and temperature. Figure 3(a) shows the electron number density profile for given values of $\mu = 0.3$ and $\theta = 0.2$. This figure illustrates some interesting features of half-space plasmon excitations at equilibrium temperature. It is remarked that electrons are significantly depleted and consequently a plasmon boundary forms just before the physical edge due to the accumulation of electrons before the boundary. The second feature which is quite unique to this model is the well-defined periodic density structure in the electron gas region ($x < 0$) which is obviously due to resonant interaction between single electron and collective excitations. Such feature has been shown to be also characteristics of an electron gas confined in an infinite potential well [76]. Finally, another remarkable feature is that well beyond the jellium edge ($x > 0$), small density hump appears resembling the electron spill out effect. However, as it is evident the electron density in our model appears as an electron halo rather than continuous spill out of electrons. The halo evidently forms due with the depleted region just before the hump and well beyond the jellium boundary. The later is a very important feature with a far reaching consequences for hot electron formation and bound state at beyond surface of perfectly conducting metallic elements or nanoparticle boundaries, as is further discussed in the following. The envelop structure of density profile looks quite similar to those discussed in many literature [97, 98]. However, the periodic fine structure is missing in other models. Figure 3(b) depicts the electrostatic energy profile corresponding to values used in Fig. 3(a). It is seen that the periodic structure is also present for this case. Close to the jellium boundary the amplitude of electrostatic energy is slightly increased and beyond the boundary the potential energy exponentially decreases towards infinity. Figure 3(c) and 3(d) depict the normalized equilibrium state function profiles for increased value of

fractional electron temperature. It is evident from Fig. 3(c) that the plasmon boundary height increases and the electron depletion after the plasmon edge becomes shallower as θ increases. Note the formation of a well-defined surface dipole just before the jellium edge. It is also remarked that electron halo density increases significantly due to increase of the normalized temperature. Quite similar trend appears for the electrostatic energy profile in elevated temperature values, θ .

Figure 4 depicts the scaled variations of equilibrium density and electrostatic energy beyond the physical boundary, $x > 0$. Figure 4(a) shows that the density profile has a dual peak structure with the first smaller peak due to electron spill-out which is merged into the boundary while the second larger peak (hot electron halo) is almost detached from boundary and extends towards infinity. The increase of the parameter, θ , leads to significant increase in the amplitude of the hot electron halo as well as the smaller peak maximum, with almost no effect on the position of the maximum amplitudes. The scaled electrostatic energy profile for the same parameter variations as in Fig. 4(a) is depicted in Fig. 4(b). It is remarked that the electrostatic energy profile has a flat-top structure near the boundary with surface value strongly dependent on the fractional temperature. Figures 4(c) and 4(d) show these profiles for the variations in normalized chemical potential of the electron gas. It is remarked that increase in the value of the chemical potential with, θ , being fixed leads to an increase in the amplitude of hot electron halo density shifting the maximum amplitude close to the jellium boundary. However, such variations in the chemical potential of the electron gas has insignificant effect on the smaller density peak. It is interesting that for higher values of μ , which coincides with that of the metallic compounds, Friedel-like oscillations in density [40] appears in front of the hot electron halo. This feature is quite similar to the positive charge screening in quantum plasmas. Effect of the change in normalized chemical potential on electrostatic energy profile for similar parameter values as in Fig. 4(c) is shown in Fig. 4(d). It is seen that increase in the chemical potential of the gas leads to significant increase in potential energy decay while for fully degenerate electron gas, with higher chemical potential values, a pronounced bound state valley forms which has a shape quite similar to the Lennard-Jones attractive potential with a distances few ten to hundred nanometers away from the boundary. This feature also is quite similar effect as previously studied quantum charge screening in plasmas [77, 83]. The existence of bound state beyond the perfectly conducting metallic surfaces together with the surface dipole

effect may be appropriate to explain the Casimir effect and less understood Casimir-Polder forces [99–101].

Figure 5 shows the detailed variations of the electrostatic potential valley profile with the change in fractional temperature and normalized chemical potential. Figure 5(a) shows that increase of the normalized temperature for fixed value of the chemical potential leads to significant decrease of bound potential energy valley without affecting the minimum position. On the other hand, Fig. 5(b) indicates that the increase of the chemical potential for fixed normalized electron gas temperature leads to increase in depth of the attractive potential valley, moving the potential minimum closer to the boundary. Figures 5(c) and 5(d) show the variations of θ and μ with respect to the electron number density of the electron gas. In terms of θ and μ the electron number density can be written as $n_0(\mu, \theta) = n_p \theta^6 \text{Li}_{3/2}[-\exp(2\mu/\theta)]^4$ with $n_p = 16e^6 m_e^3 / (\pi^3 \hbar^6) \simeq 5.66 \times 10^{19} \text{cm}^{-3}$ being the characteristic plasmon number-density. According to Fig. 5(c) almost independent of the value of θ the metallic density is universal in $\mu > 1$ region. It is therefore concluded that the bound potential valley should be present for electron densities relevant also for strongly doped N-type semiconductors beside the known metals such as for a Schottky contact. It is further concluded from Fig. 5(d) that for very high values of θ the electron density approaches the value for fully degenerate gas where the bound potential should be present.

Current model may also be used for alternative description of the hot electron generation mechanism via surface plasmonic excitations in nanometallic compounds. The hot electron generation via LSPR phenomenon is a new efficient method of electricity production from localized high energy UV-VIS electromagnetic radiation [20]. The schematic diagram of hot electron generation is depicted in Fig. 6(a). The Fermi energy (zero chemical potential) level coincides with $E = 0$ and the Fermi sea of electrons remain under this energy level. Figure 6(a) also shows the normalized free electron ($E = k^2/2$) dispersion (in red) and the plasmon ($E = (1 + k^4)/2k^2$) dispersion (in blue). The dual scale-length character of plasmon excitations is evident from the corresponding curve for given energy $E > 2E_p$. The plasmon dispersion curve consists of two distinct branches of low and high phase-speed excitations with respectively positive and negative group velocities. The plasmon dispersion approaches asymptotically to the free electron curve in the low phase-speed limit. For the purpose of hot electron generation the high energy electromagnetic radiation on the metallic surface can excite electrons of the Fermi sea to finite width plasmonic band which

is called the hot electron band. Note that, presence of such a finite lifetime plasmonic band structure is necessary for high energy collective stir up of electromagnetically excited electrons. It is noted that only radiation with energies $\hbar\omega \geq 2E_p$ is able to excite electrons to hot electron band with effective maximum width, E_F . For conventional nanometallic materials such as silver and gold the corresponding plasmon energies are $E_p = 9.01\text{eV}$ and $E_p = 9.03\text{eV}$ [102], respectively, which amount to minimum electromagnetic energy of $\hbar\omega \simeq 18\text{eV}$ ($\lambda \simeq 68.9\text{nm}$) residing well in the UV spectrum. Intraband and interband transitions may also be alternative low energy excitation of Fermi electrons leading to escape of energetic electrons from the surface (or Schottky) potential barrier, Φ_s [20]. However, for ultrahigh energy electron extraction the hot electron plasmonic band formation is a necessary condition.

Collective excitations may decay through various channels in metallic nanoparticle LSPR [27]. These decays are of the radiative and nonradiative types [20]. In a radiative type decay the electromagnetically excited electrons reemit radiation which is either absorbed by the material causing the heat production or due to finite width of hot electron band leads to the photochromism effect [103]. The electromagnetic decay causing the photochromism occur at timescale of the femtosecond order [104]. The electron-electron and electron phonon scattering and Landau damping phenomenon are of the most effective decay types. The electron-electron scattering are strongly lowered in metallic compound by the well-known Pauli-Blocking [70]. Moreover, the electron-phonon scattering are rare in highly ordered crystalline material but can play dominant role in glasses [32]. In current model electron-phonon coupling is ignored due to the fact that ion dynamics is not considered in the jellium model. However, in recent investigations, consideration of dynamic ions shows its fundamental contributions to the low energy plasmon band structure [105]. It is therefore possible for low energy phono-assisted plasmon excitations in the presence of dynamic ions. The Landau damping is one of well studied phenomena in physics [106]. It is known to occur due to wave-particle interactions in electron plasma oscillations. A classical interpretation of the Landau damping follows that particles with speed slightly less than the plasmon phase-speed extract energy from the wave and viceversa. Since the population of low speed electrons is larger than those with high speed ones in the distribution, the plasmon excitation is rapidly damped. The Landau damping rate is directly related to the hot electron extraction in plasmonic materials which is an important parameter in photovoltaic device efficiency. The

nonradiative decay of hot electrons into the free electron band, consequently, leads to escape of hot electrons with energies exceeding that of the Schottky barrier potential, as depicted in Fig. 6(a). The energy distribution of hot electrons in plasmonic band is shown in Fig. 6(b) for different values of the normalized temperature, as given by $dn(E)/dE \simeq D(E)f_B(E)$ with $D(E)$ being the plasmon density of states and $f_B(E)$ is the Maxwell-Boltzmann distribution function for dilute hot electrons in plasmonic band. The hot electron energy band extends from $E_{min} \geq 1$ up to the electromagnetic wave energy $\hbar\omega$. In case the hot electron band completely takes place inside the plasmon band, we have $E_{min} = \hbar\omega - E_F$. Therefore, the number density of hot electrons (normalized to the equilibrium electron number density of Fermi gas) in the band is given by

$$n = \int_{E_{min}}^{\hbar\omega} f_B(\mu, \theta) D(E) dE, \quad (13)$$

which is the area under the curves in Fig. 6(b). It is however remarked that with increase in the electron gas temperature the number of hot electrons increases significantly. As remarked before, the decay time is a determining parameter in hot electron generation of photovoltaic devices. It has been shown that the Landau damping rate in spherical nanometallic particles has inverse dependence to the particle radius (R) [31]. The damping rate $\Gamma(R) = \Gamma_\infty + \Gamma_L(R)$ consists of the resistive Drude damping (Γ_∞) and Landau wave-particle damping $\Gamma_L(R) = Av_F/R$ contributions, in which A is a constant dependent to particle geometry and v_F is the Fermi speed [31]. It is evident that in the large particle limit $R \rightarrow \infty$ the Landau damping vanishes and the dielectric properties of metallic compounds shows Drude-like behavior. It is seen that smaller metallic nanoparticles are more efficient for hot electron regeneration because of higher plasmonic damping character. Therefore, the efficient plasmonic photovoltaic devices should be composed of nanometallic particles with smaller size but higher electron concentration. It is interesting that these devices operate more efficient at higher temperatures unlike their semiconductor counterparts. Our model may also be appropriate for description of plasmon excitations in a two dimensional electron gas (2DEG) and high electron concentrated gapped graphene. However, the collective excitations of massless Dirac hot electron generation in two dimensional materials like intrinsic graphene and silicene requires further development of appropriate hydrodynamic models. For this purpose one needs to use the appropriate kinetic theory to obtain pseudo-

force model from hydrodynamic equations of doped (metallic) graphene. One such a model of Dirac electron hydrodynamic has been recently derived in Ref. [107].

IV. CONCLUSION

In current research we developed a theoretical model to study the half-space plasmonic excitations in an electron gas of arbitrary degeneracy. We used the linearized Schrödinger-Poisson model and reduced the system it to the coupled pseudoforce type second-order differential equations, solutions of which with and without damping effects is used to construct the appropriate state functions for half-space electron gas excitations in different spatial regions. Current dual-tone theory of plasmon excitations may fully captures essential electrostatic interactions between single electrons and the collective entity. Some novel features of half-space plasmonic excitation were coined in this research and its relevance to plasmonic hot electron generation was discussed in detail. A Lennard-Jones-like bound electrostatic potential energy valley forms beyond the physical boundaries in fully degenerate electron gas which may characterize the Casimir effects. Current study may also be extended to study the half-space plasmon excitations in other geometries such as spherical geometry in order to study the microscopic forces among metallic nanoparticles.

V. DATA AVAILABILITY

The data that support the findings of this study are available from the corresponding author upon reasonable request.

-
- [1] G. Manfredi, Phys. Plasmas **25**, 031701(2018); <https://doi.org/10.1063/1.5026653>
 - [2] S. A. Maier, Plasmonics: Fundamentals and Applications, Springer Science Business Media LLC (2007).
 - [3] H. Haug and S. W. Koch, "Quantum theory of the optical and electronic properties of semiconductors", World Scientific, 2004,
 - [4] C. Gardner, SIAM, J. Appl. Math. **54** 409(1994).
 - [5] F. Wooten, Optical Properties of Solids, Academic (1972).

- [6] S. Das Sarma and A. Madhukar, Phys. Rev. B **23**, 805(1981).
- [7] F. Stern, Phys. Rev. Lett., **18** 546(1967).
- [8] E. H. Hwang and S. Das Sarma. Phys. Rev. B, **75** 205418(2007).
- [9] R. Gupta and B. K. Ridley, Phys. Rev. B **39**, 6208(1989).
- [10] S. Datta and R. L. Gunshor, J. Appl. Phys. **54**, 4453(1983).
- [11] P.A. Markovich, C.A. Ringhofer, C. Schmeister, Semiconductor Equations, Springer, Berlin, 1990.
- [12] F. F. Chen, Introduction to Plasma Physics and Controlled Fusion, 2nd ed. (Plenum Press, New York, London, 1984).
- [13] N. A. Krall and A. W. Trivelpiece, "Principles of Plasma Physics", (San francisco Press, San francisco 1986).
- [14] P. G. Drazin and R. S. Johnson, "Solitons: an introduction", Cambridge Texts in Applied Mathematics, Cambridge University Press, (1993)
- [15] Stenflo, L. 1976 Phys. Scripta 14, 320.
- [16] Stenflo, L. and Tsintsadze, N. L. 1979 Astrophys. Space Sci. 64, 513.
- [17] Stenflo, L. 1981 Phys. Scripta 23, 779.
- [18] Stenflo, L. and Shukla, P. K. 1999 Phys. Plasmas 6, 1382.
- [19] S. Ummethala, T. Harter, K. Koehnle, Z. Li, S. Muehlbrandt, Y. Kutuvantavida, J. Kermal, P. Marin-Palomo, J. Schaefer, A. Tessmann, et al., Nat. Photonics **13**, 519(2019); doi.org/10.1038/s41566-019-0475-6
- [20] C. Calvero, Nat. Photonic **8**, 95(2014).
- [21] Jacob B. Khurgin, Nanophotonics **9(2)**, 453(2020).
- [22] Wei Li and Jason G. Valentine, Nanophotonics **6(1)**, 177(2017).
- [23] Cristian Ciraci, Radoslaw Jurga, Muhammad Khalid and Fabio Della Sala, Nanophotonics **8(10)**, 1821(2019).
- [24] Mario Zapata Herrera, Javier Aizpurua, Andrey K. Kazansky, and Andrei G. Borisov, Langmuir **32**, 2829(2016).
- [25] Gregory V. Hartland, Lucas V. Besteiro, Paul Johns, and Alexander O. Govorov, ACS Energy Lett. **2**, 1641(2017).
- [26] Changhwan Lee, Yujin Parkbc and Jeong Young Park, RSC Adv. **9**, 18371(2019).
- [27] Lucas Vazquez Besteiro, Xiang-Tian Kong, Zhiming Wang, Gregory V Hartland, and Alexan-

- der O. Govorov, ACS Photonics (accepted); DOI: 10.1021/acsp Photonics.7b00751
- [28] H. A. Atwater, Sci. Am. **296**, 56(2007).
- [29] H. A. Atwater and A. Polman, Nat. Mater. **9**, 205(2010).
- [30] Y. Tian and T. Tatsuma, J. Am. Chem. Soc. **127**, 7632(2005).
- [31] Vincenzo Amendola and Moreno Meneghetti, J. Phys. Chem. C **113**, 4277(2009).
- [32] C. Hu, Modern Semiconductor Devices for Integrated Circuits (Prentice Hall, Upper Saddle River, New Jersey, 2010) 1st ed.
- [33] K. Seeger, Semiconductor Physics (Springer, Berlin, 2004) 9th ed.
- [34] S. Glenzer, O. L. Landen, P. Neumayer, R. W. Lee, K. Widmann, S. W. Pollaine, R. J. Wallace, G. Gregori, A. Höll, T. Bornath, R. Thiele, V. Schwarz, W.-D. Kräfft, and R. Redmer, Phys. Rev. Lett. **98**, 065002 (2007).
- [35] M. Koenig, A. Benuzzi-Mounaix, A. Ravasio, T. Vinci1, N. Ozaki, S. Lepape, D. Batani, G. Huser, T. Hall, D. Hicks, A. MacKinnon, P. Patel, H. S. Park, T. Boehly, M. Borghesi, S. Kar and L. Romagnani, Plasma Phys. Control. Fusion **47**, B441 (2005).
- [36] M. Bonitz, D. Semkat, A. Filinov, V. Golubnychiy, D. Kremp, D. O. Gericke, M. S. Murillo, V. Filinov, V. Fortov, W. Hoyer, J. Phys. A, **36** 5921(2003).
- [37] James P. Mithen, Jérôme Daligault, and Gianluca Gregori, Phys. Rev. E **82** 015401(R) (2012).
- [38] S. Chandrasekhar, "An Introduction to the Study of Stellar Structure", Chicago, Ill. (The University of Chicago press), (1939), p.392.
- [39] C. Kittel, Introduction to Solid State Physics, (John Wiley and Sons, New York, 1996), 7th ed.
- [40] N. W. Ashcroft and N. D. Mermin, Solid state physics (Saunders College Publishing, Orlando, 1976).
- [41] E. Madelung, Z. Phys., 40 322(1926).
- [42] E. Fermi and E. Teller, Phys. Rev. **72**, 399 (1947).
- [43] F. Hoyle and W. A. Fowler, Astrophys. J. **132**, 565(1960).
- [44] S. Chandrasekhar, "An Introduction to the Study of Stellar Structure", The University of Chicago Press, Chicago (1939).
- [45] D. Bohm and D. Pines, Phys. Rev. **92** 609(1953).
- [46] Bohm, D. Phys. Rev. **85**, 166–179 (1952).

- [47] Bohm, D. Phys. Rev. **85**, 180–193 (1952).
- [48] D. Pines, Phys. Rev. **92** 609(1953).
- [49] P. Levine and O. V. Roos, Phys. Rev, **125** 207(1962).
- [50] Y. Klimontovich and V. P. Silin, in Plasma Physics, edited by J. E. Drummond (McGraw-Hill, New York, 1961).
- [51] S. Ichimaru, Rev. Mod. Phys. **54**, 1017 (1982).
- [52] S. Ichimaru, H. Iyetomi, and S. Tanaka, Phys. Rep. **149**, 91 (1987).
- [53] S. Ichimaru, *Statistical Physics: Condensed Plasmas* (Addison Wesley, New York, 1994).
- [54] V. E. Fortov and I. T. Iakunov, *The Physics of Non-Ideal Plasmas* (World Scientific, Singapore, 1999).
- [55] V. E. Fortov, Phys. Usp. **52**, 615 (2009).
- [56] R. Redmer, Phys. Rep. **282**, 35 (1997); S. Eliezer, P. Norreys, J. T. Mendonça, and K. Lancaster, Phys. Plasmas **12**, 052115 (2005).
- [57] Weitao Yang, Phys. Rev. A **34**, 4575(1986).
- [58] P. K. Shukla and B. Eliasson, Phys. Rev. Lett. **99**, 096401(2007).
- [59] L Stenflo Phys. Scr. **T50** 15(1994).
- [60] P. K. Shukla, B. Eliasson, and L. Stenflo Phys. Rev. E **86**, 016403(2012).
- [61] F. Haas, *Quantum Plasmas: An Hydrodynamic Approach* (Springer, New York, 2011).
- [62] G. Brodin and M. Marklund, New J. Phys. **9**, 277(2007).
- [63] M. Marklund and G. Brodin, Phys. Rev. Lett. **98**, 025001(2007).
- [64] N. Crouseilles, P. A. Hervieux, and G. Manfredi, Phys. Rev. B **78**, 155412 (2008).
- [65] Z. Moldabekov, Tim Schoof, Patrick Ludwig, Michael Bonitz, and Tlekkabul Ramazanov, Phys. Plasmas, **22**, 102104(2015); doi.org/10.1063/1.4932051
- [66] L. Stanton and M. S. Murillo, Phys. Rev. E **91**, 033104(2015).
- [67] F. Haas, G. Manfredi, P. K. Shukla, and P.-A. Hervieux, Phys. Rev. B, **80**, 073301 (2009).
- [68] B. Eliasson and P. K. Shukla, Phys. Scr. **78**, 025503 (2008).
- [69] Hwa-Min Kim and Young-Dae Jung, EPL, **79** 25001(2007).
- [70] G. Manfredi, “How to model quantum plasmas,” Fields Inst. Commun. **46**, 263–287 (2005); in Proceedings of the Workshop on Kinetic Theory (The Fields Institute, Toronto, Canada 2004): <http://arxiv.org/abs/quant-ph/0505004>.
- [71] F. Haas, *Quantum Plasmas: An Hydrodynamic Approach* (Springer, New York, 2011).

- [72] G. Manfredi and F. Haas, Phys. Rev. B **64**, 075316 (2001);
- [73] G. Manfredi, **86**(2), 825860201(2020); doi:10.1017/S0022377820000240
- [74] J. Hurst, K. L. Simon, P. A. Hervieux, G. Manfredi and F. Haas, Phys. Rev. B **93**, 205402(2016).
- [75] M. Akbari-Moghanjoughi, Phys. Plasmas **25**, 102105(2018); doi: 10.1063/1.5055372
- [76] M. Akbari-Moghanjoughi, Phys. Plasmas, **26**, 012104 (2019); doi.org/10.1063/1.5078740
- [77] P. K. Shukla and B. Eliasson, Phys. Rev. Lett. **108**, 165007 (2012); **108**, 219902 (E) (2012); *ibid.* **109**, 019901 (E) (2012).
- [78] M. Bonitz, E. Pehlke, and T. Schoof, Phys. Rev. E **87**, 033105 (2013).
- [79] P. K. Shukla, B. Eliasson, and M. Akbari-Moghanjoughi, Phys. Rev. E **87**, 037101 (2013).
- [80] M. Bonitz, E. Pehlke, and T. Schoof, Phys. Rev. E **87**, 037102 (2013).
- [81] P. K. Shukla, B. Eliasson and M. Akbari-Moghanjoughi, Phys. Scr. **87** 018202 (2013).
- [82] M. Bonitz, E. Pehlke, and T. Schoof, Phys. Scr. **88**, 057001 (2013).
- [83] M. Akbari-Moghanjoughi, Phys. Plasmas **22**, 022103 (2015); *ibid.* **22**, 039904 (E) (2015).
- [84] Zh. Moldabekov, T. Schoof, P. Ludwig, M. Bonitz, and T. Ramazanov, Phys. Plasmas **22**, 102104 (2015).
- [85] D. Michta, F. Graziani, and M. Bonitz, Contrib. Plasma Phys. **55**, 437 (2015).
- [86] M. Akbari-Moghanjoughi, Phys. Plasmas **27**, 042107 (2020); doi.org/10.1063/5.0004857;
- [87] M. Akbari-Moghanjoughi, Phys. Plasmas, **26**, 072106 (2019); doi.org/10.1063/1.5097144
- [88] M. Akbari-Moghanjoughi, Phys. Plasmas, **26**, 062105 (2019); doi.org/10.1063/1.5090366
- [89] M. Akbari-Moghanjoughi, Phys. Plasmas, **26**, 112102 (2019); doi.org/10.1063/1.5123621
- [90] M. Akbari-Moghanjoughi, Phys. Plasmas, **26**, 022110 (2019); doi.org/10.1063/1.5087201
- [91] M. Akbari-Moghanjoughi, Phys. Plasmas, **26**, 022111 (2019); doi.org/10.1063/1.5083150
- [92] M. Akbari-Moghanjoughi, Phys. Plasmas, **26**, 052104 (2019); doi.org/10.1063/1.5080347
- [93] M. Akbari-Moghanjoughi, Phys. Plasmas, **26**, 062110 (2019); doi.org/10.1063/1.5098054
- [94] Setsuo ICHIMARU, Hiroshi IYETOMI and Shigenori TANAKA, Phys. Rep. **205**, 91(1987).
- [95] H. Nikolic, Found. Phys. Lett. **17** 363(2004).
- [96] Y. Couder, A. Boudaoud, S. Protière, J. Moukhtar, E. Fort, Europhysics News. **41** 14(2010).
- [97] Cristian Ciraci, Radoslaw Jurga, Muhammad Khalid and Fabio Della Sala, Nanophotonics **8**(10), 821(2019);doi.org/10.1515/nanoph-2019-0199
- [98] Mario Zapata Herrera, Javier Aizpurua, Andrey K. Kazansky, and Andrei G. Borisov, Lang-

- muir **32**, 2829(2016); doi:10.1021/acs.langmuir.6b00112
- [99] Hrvoje Nikolic, *Annals of Physics* **383**, 181(2017).
- [100] Hrvoje Nikolic, *Physics Letters B* **761**, 197(2016).
- [101] G. Bressi, G. Carugno, R. Onofrio, and G. Ruoso, *Phys. Rev. Lett.* **88**, 041804(2002).
- [102] Aleksandar D. Rakic, Aleksandra B. Djuris, Jovan M. Elazar, and Marian L. Majewski, *Appl. Optics*, **37(22)** 5271(1998).
- [103] Y. Ohko, Yoshihisa Ohko, Tetsu Tatsuma, Tsuyoshi Fujii, Kenji Naoi, *Nat. Mater.* **2**, 29(2003).
- [104] C. Sonnichsen, T. Franzl, T. Wilk, G. von Plessen, J. Feldmann, O. Wilson, and P. Mulvaney, *Phys. Rev. Lett.* **88**, 077402(2002).
- [105] M. Akbari-Moghanjoughi, arXiv:2009.08098 [physics.plasm-ph] (under review).
- [106] Tigran V. Shahbazyan, *Phys. Rev. B* **94**, 235431(2016).
- [107] Bengt Eliasson, and Chuan Sheng Liu, *Phys. Plasmas* **25**, 012105(2018).

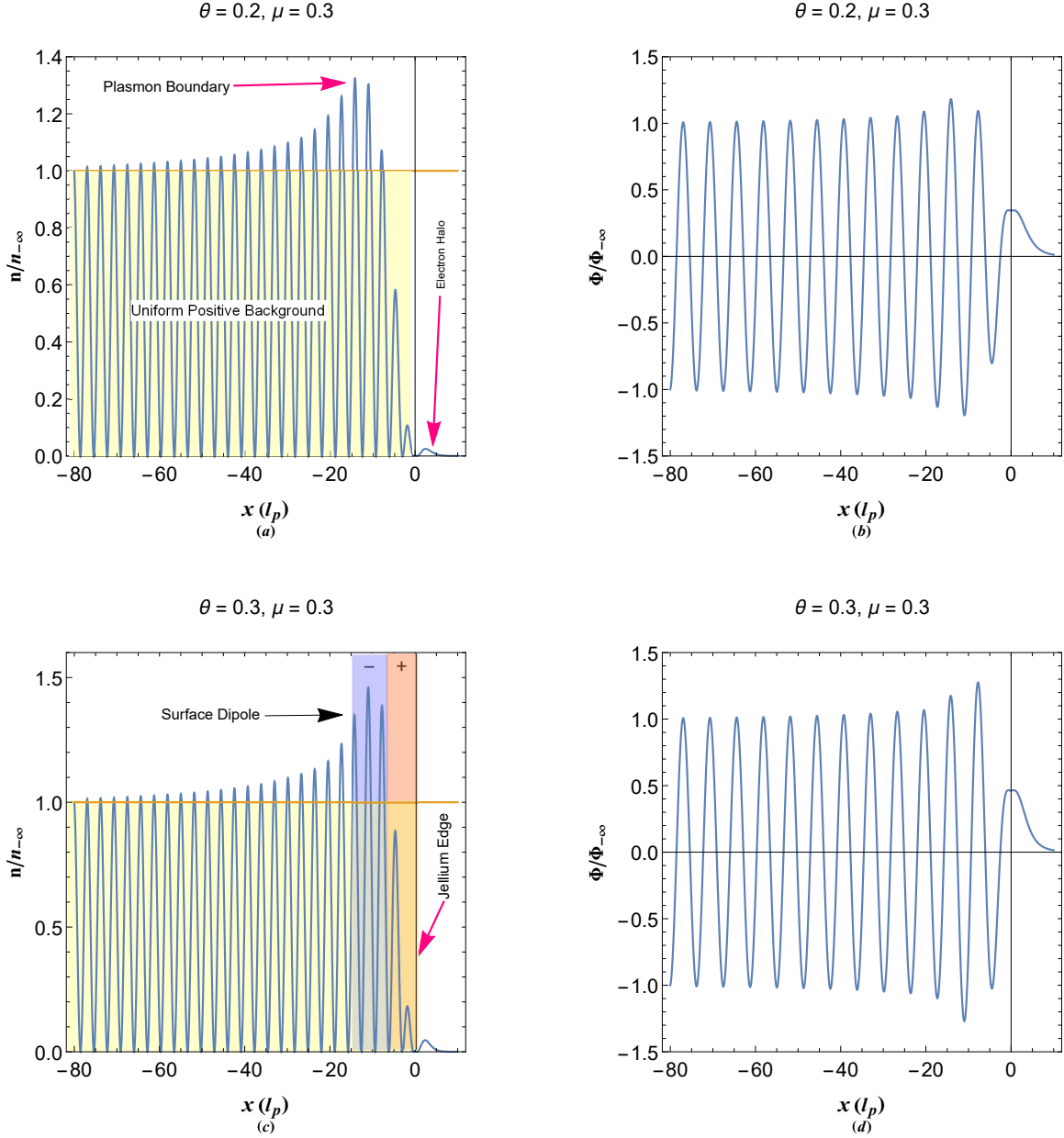


FIG. 3: 3(a) and 3(c) Show statistically averaged values of normalized perturbed electron number-density. 3(b and 3(d)) Show normalized perturbed electrostatic potential energy for electron gas-vacuum half-space plasmon excitations at a thermal equilibrium condition for given parameter values of θ and μ . The boundary at $x = 0$ separates the uniform positive background charge (shaded area) from the vacuum (unshaded region) in plots 3(a) and 3(c).

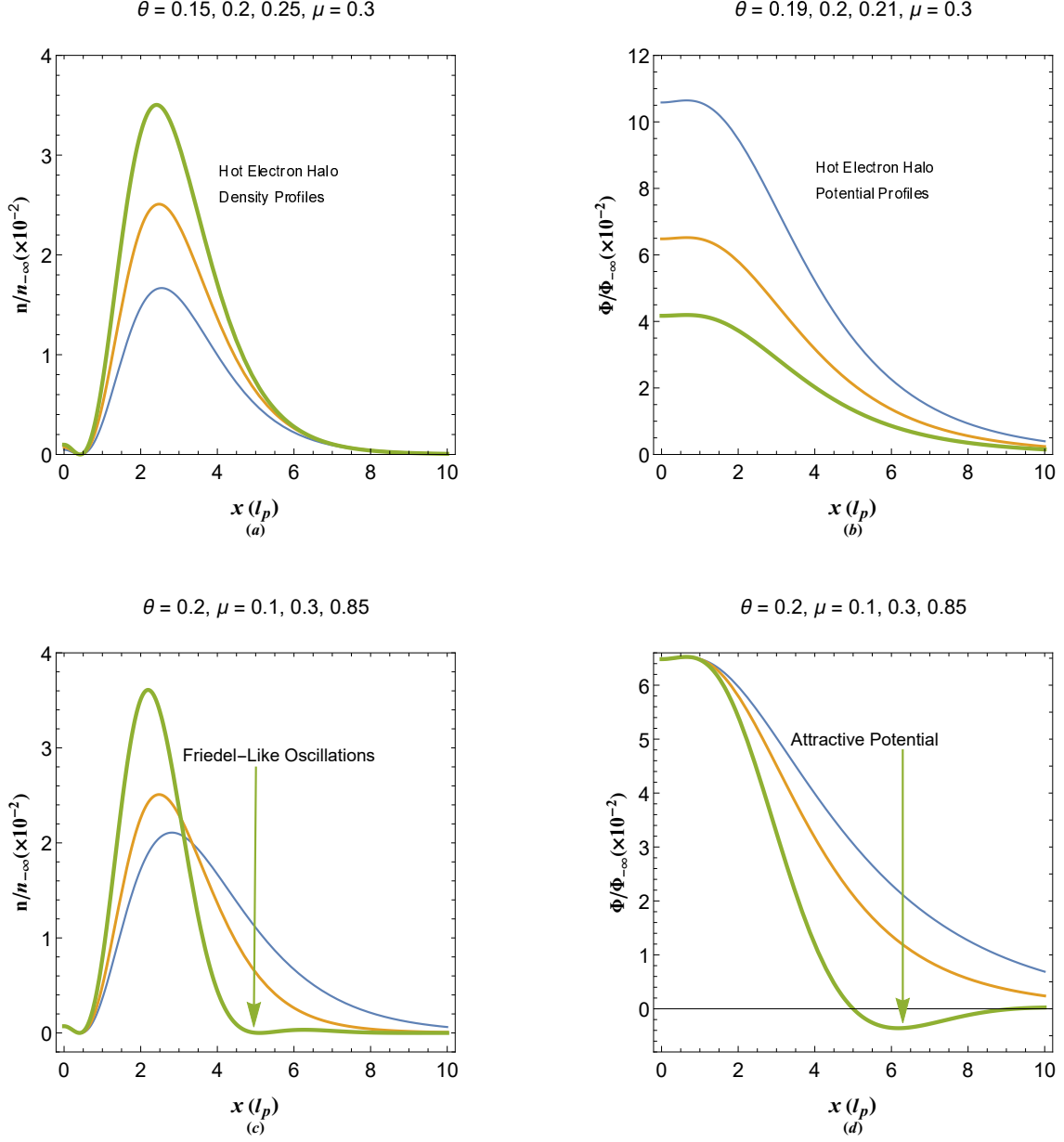


FIG. 4: 4(a) and 4(c) The scaled variations of equilibrium electron number density. 4(b) and 4(d) The electrostatic potential energy in the vacuum side for different values of the normalized electron temperature and chemical potential. The increase in the thickness of curves in each plot is meant to represent an increase in the varied parameter above each panel.

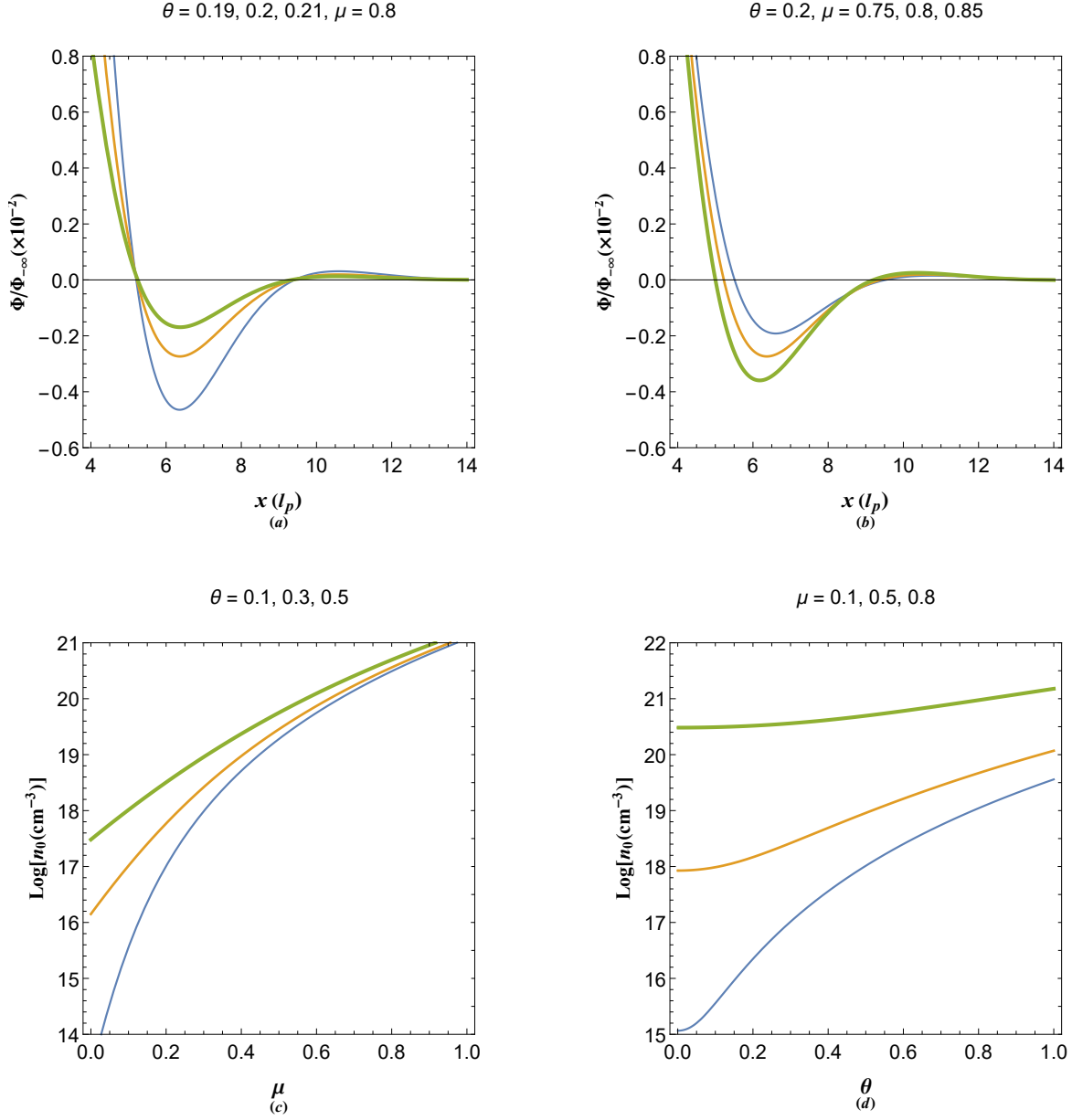


FIG. 5: 5(a) Changes in the bound electrostatic energy valley with the change in the fractional electron temperature. 5(b) Variations in the bound electrostatic energy valley with changes in the normalized chemical potential of the electron gas. 5(c) Variation of the electron number density with normalized chemical potential for different values of electron number density. 5(d) Variation of the normalized electron temperature with normalized chemical potential for different values of normalized electron temperature. The increase in the thickness of curves in each plot is meant to represent an increase in the varied parameter above each panel.

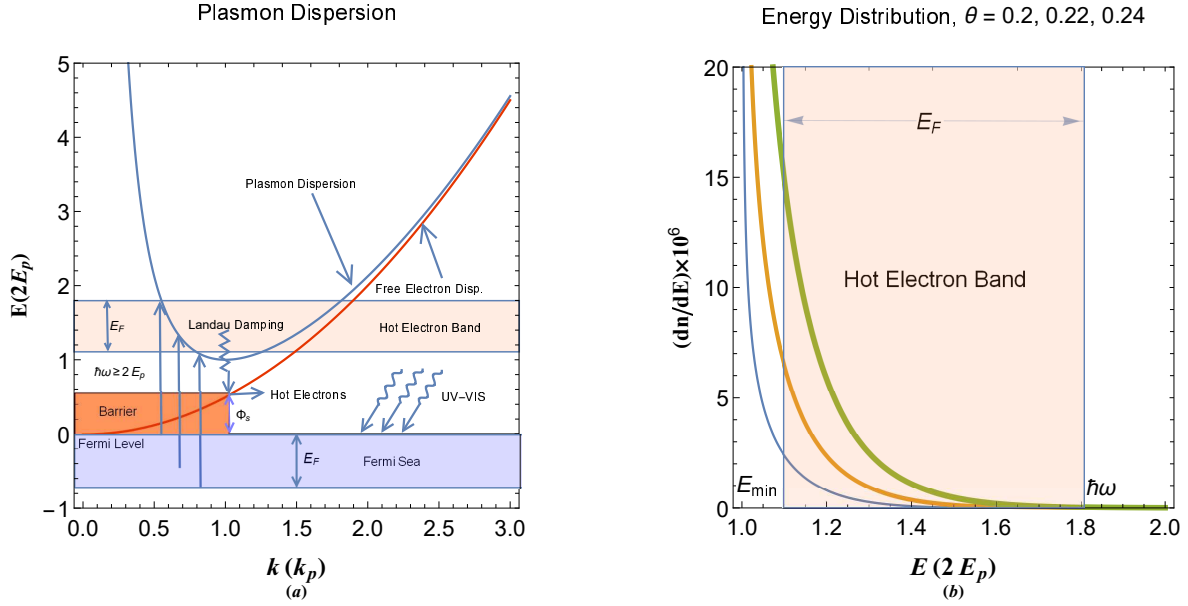


FIG. 6: 6(a) The schematic description of hot electron dynamics in the plasmon band structure. 6(b) The energy spectrum of hot electrons at different normalized temperature. The increase in the thickness of curves in 6(b) represents an increase in the varied parameter above each panel.